A Kinematical Detection of Two Unseen Jupiter Mass Embedded Protoplanets

Richard D. Teague[*,1], Jaehan Bae[2], Edwin A. Bergin[1], Tilman Birnstiel[3] & Daniel Foreman-Mackey[4]

[1]*Department of Astronomy, University of Michigan, 311 West Hall, 1085 S. University Ave, Ann Arbor, MI 48109, USA*

[2]*Department of Terrestrial Magnetism, Carnegie Institution for Science, 5241 Broad Branch Road, NW, Washington, DC 20015, USA*

[3]*University Observatory, Faculty of Physics, Ludwig-Maximilians-Universität München, Scheinerstr. 1, D-81679 Munich, Germany*

[4]*Center for Computational Astrophysics, Flatiron Institute, 162 5th Ave, New York, NY 10010*

Planets form deep within the midplane of protoplanetary disks consisting of circumstellar material that orbits a young star. Substructure in the disk, such as spirals and rings, appears ubiquitous in the thermal emission arising from mm-sized solid particles. This has been argued to indicate the presence of hidden planets[1–4]. Relating substructure in thermal emission to potential planet masses and locations is highly uncertain due to ill-constrained gas-to-dust ratios and optical properties for the dust. Interpretation is further hampered by grain evolution and gas dynamical effects which result in similar substructure without the need for the presence of a planet[5–9]. Here we report the first kinematical evidence of two embedded Jupiter-mass planets in the disk around the young star HD 163296 at 100 au and

165 au. By detecting small changes in rotation velocity of the gas arising from local gas pressure gradient changes, we are able to constrain the embedded planet mass and location to an exceptional precision of $\sim$50% and $\sim$10%, respectively. This method opens up a new avenue for the exploration of planetary systems into the formative stages.

To date over 3700 planets have been detected[10] with the first detections obtained by utilizing the gravitational influence of the planet on the star inducing velocity shifts via the Doppler effect. Planet detection during the formative stages is more challenging. There are a handful of claimed detections via direct imaging[11–14], but the vast majority of planets remain hidden; their presence inferred from visual evidence of gaps and rings seen in the thermal continuum emission of dust[1,3,15]. Subsequent determination of the properties of the planet is limited by the fact that estimates of the gas density from the dust is fraught with uncertainties[16]. Ill-constrained gas-to-dust ratios and complex grain evolution folded into commonly used analytical formulae relating dust gap width and depth to planet mass culminate in errors of the planet mass of up to 200%[17–19]. Furthermore, it has been shown that a gap does not directly infer the presence of a planet. Massive planets are able to excite spiral waves which open up secondary and tertiary gaps[9], while grain growth around ice-lines and the shepherding of dust by (magneto-)hydrodynamical instabilities have also been shown to produce ring-like structures[5–8]. In all, while hidden planets are the preferred interpretation of structure seen in dust emission maps, current methods do not robustly distinguish between scenarios nor provide reliable constraints for embedded planet masses.

We use archival Atacama Large Millimetre Array (ALMA) data of HD 163296 which shows ring structure in the mm continuum which have been used to infer the presence of at least two planets at 100 and 165 au[3]. We use the CO isotopologue emission to detected deviations from Keplerian rotation across these continuum features. Such deviations are consistent with changes in the local pressure gradient expected from significant perturbations in the surface density of the disk[20]. Comparison with hydrodynamical simulations show that a $1\ M_{\mathrm{Jup}}$ planet at 100 au and a $1.3\ M_{\mathrm{Jup}}$ planet at 165 au are driving the two outer perturbations, while the inner perturbation is either a smaller mass $0.6\ M_{\mathrm{Jup}}$ planet at $\sim$65 au, or the outer edge of the magneto-rotational instability (MRI) deadzone. At such large distances from the star these planets result in a minimal effect on the stellar velocity, however deviations in the local gas velocity structure betray their presence.

With the high sensitivity and fine velocity resolution ($50\ \mathrm{m\,s^{-1}}$) afforded by ALMA we are able to constrain the centroid of emission to an precision of $8\ \mathrm{m\,s^{-1}}$, or 0.3% of the projected Keplerian rotation velocity at 150 au, and thus derive an exceptionally precise rotation curve (see the Methods section for the calibration of this precision). Comparison of this rotation curve with a Keplerian profile assuming a stellar mass of $2.3\ M_{\mathrm{sun}}$ and a disk inclination of $i = 47.7^{\circ}$ shows significant (up to 6σ) residuals as shown in Figure 1.

Despite the velocity signatures, no clear substructure is observed in the radial profile of the integrated $C^{18}O$ emission shown in panel (*a*), suggesting no significant changes in optical depth of the emission. However, the emission surface of $C^{18}O$ dips at the locations of the dark rings observed in the continuum emission, the causes of which are discussed in the Methods section.

The rotation curve in panel (c) is well matched by a Keplerian profile, however the residual, shown in panel (d), clearly exhibits significant deviations. Comparable perturbations are observed in ^{12}CO and ^{13}CO emission and are discussed in the Methods section. The substantial deviation in the inner disk ($r < 70$ au) is likely due to the spatial resolution of the data (≈ 31 au), while the locations and amplitudes of the outer features are consistent with predictions for planet driven perturbations[20].

Particles which have grown large enough to decouple from the gas will rotate with a Keplerian velocity, $v_{\rm Kep} = \sqrt{GM_\star \, / \, r}$. On the other hand, gas, as traced with molecular line emission, is in both radial and vertical hydrostatic equilibrium. As such, the radial pressure gradient supports the gas against the gravitational pull of the central star, slowing the rotation[21,22]. For a geometrically thick disk, the rotation velocity $v_{\rm rot}$ at a given point within the disk is given by,

$$\frac{v_{\rm rot}^2}{r} = \frac{GM_\star r}{(r^2 + z^2)^{3/2}} + \frac{1}{\rho_{\rm gas}} \frac{\partial P}{\partial r} \tag{1}$$

where $M_\star$ is the mass of the star and $\partial P \, / \, \partial r$ is the radial pressure gradient. In this we have not included the gravitational component of the disk as this will only introduce a linear trend and modelling it would require a well constrained gas mass for the disk[21]. Over small scales changes in $v_{\rm rot}$ will therefore be due to changes in the emission height, z, or changes in the local pressure gradient.

Local changes in the emission height as the sole reason can be ruled out as comparable perturbations are seen in all three isotopologes, despite a change in height only observed for C^{18}O.

Rather the deviations are likely due to changes in the local pressure gradient, such as from a gap carved by an embedded protoplanet[19]. This scenario gives rise to a distinct perturbation from a smooth rotation curve: rotation is slowed on the inner side of the perturbation, and hastened on the outer side as shown in Figure 2c. Residuals in the rotation profile agree with this scenario: gaps in the continuum at 60, 100 and 160 au are bounded by a local minimum inwards of the gap and a local maximum outside the gap (although the local minima inwards of 60 au is not observed due to the spatial resolution of the data).

To test this hypothesis, we ran hydrodynamical models of embedded protoplanets guided by the best-fit values inferred from the continuum rings[3]. We limit ourselves to comparisons with the $C^{18}O$ emission as this is originating from the densest region of the disk and least likely to be affected by the poorly constrained physical structure of the upper disk. We find excellent agreement with the two outer gaps with planets at 100 au and 165 au with masses of $1\ M_{\rm Jup}$ and $1.3\ M_{\rm Jup}$, respectively, as shown in Figure 2. Altering the mass and radial position of these two planets we are able to constrain the planet masses to 50% and their radial location to 10% given the current uncertainties on $\delta v_{\rm rot}$.

Determining the source of the inner-most perturbation is more complex. As noted in previous studies[3], the continuum ring is too wide to be well described by a single embedded planet. From our hydrodynamic simulations we are unable to find as a convincing fit as the outer planets, but the inner feature is qualitatively well described by a $0.6\ M_{\rm Jup}$ planet a 65 au. An alternative scenario proposed for the inner gap in continuum emission is the pressure confinement of grains at 80 au due to the edge of the deadzone of the magneto-rotational instability (MRI)[6,23]. Such pressure confinement would require a pressure maximum at the centre of the bright ring leading to a local maximum in $\delta v_{\rm rot}$ inwards of that location, consistent with the observations.

The observed rotation curve, and thus the inferred pressure gradient, requires the disk to possess a surface density structure comparable to that in Figure 3a. Other hydrodynamical instabilities have been shown to result in surface density perturbations, such as the MRI, zonal flows, the vertical shear instability[24–27]. Tight constraints on the turbulence in the disk[28,29] limit the strength of these instabilities, resulting in long viscous time scales, considerably older than the age of the disk. Furthermore, many of these instabilities are transient, however to be applicable for HD 163296 must be sufficiently long lived enough to drive the continuum substructure we observe. Until there are firm predictions for the rotational profiles expected from these instabilities, embedded planets remain the favoured scenario, naturally recovering all observations.

With these observations we have presented the first kinematical evidence of embedded protoplanets in a protoplanetary disk. In Figure 4 we compare these planets to the current state of existing planet detections. Our planets are younger (estimated age of $\lesssim$ 5 Myr[30]) and open a new area of parameter space, hinting at the presence of a population of distant Jupiter mass planets. This method provides the first opportunity to inventory the systems which harbour on-going planet formation. In the future the presence of these planets, which retain heat at formation, may be confirmed by sensitive mid-infrared facilities such as the James Webb Space Telescope. Just as important, we have only begun to grasp the potential of ALMA for planet detection and the use of

Doppler planet detection into a new realm.

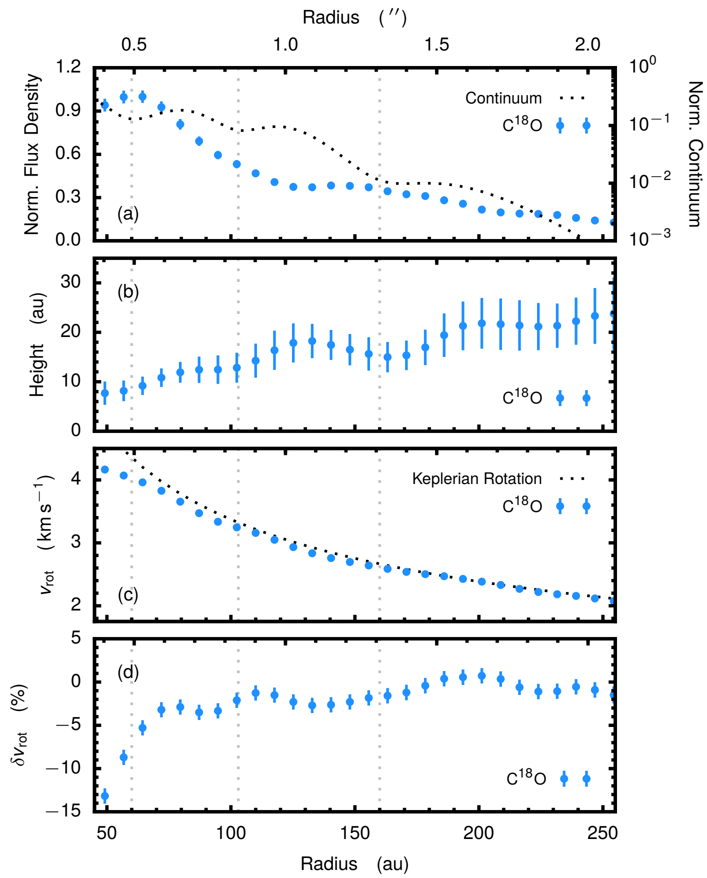

Figure 1: **$C^{18}O$ observations of HD 163296**. Panel (*a*) shows the normalised radial profile of the $C^{18}O$ flux density and the logarithm of the continuum density model[3] as the dotted curve. The derived emission surface and rotation velocity, $v_{\rm rot}$, are shown in panels (b) and (c), respectively. The relative deviation, $\delta v_{\rm rot}$, from the reference Keplerian rotation curve shown by the dotted line, is displayed in the bottom panel. All panels show Gaussian Process models of the data with associated 3σ error-bars. The dotted vertical lines show the location of the dark rings in the continuum emission [3].

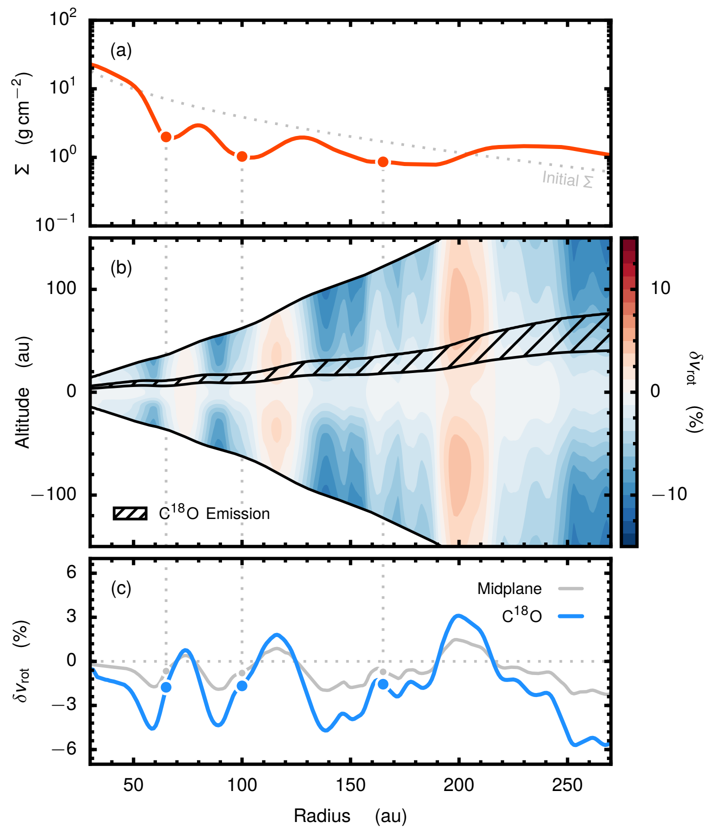

Figure 2: **Best-fit disk physical structure**. The azimuthally averaged surface density from the best-fit hydrodynamical model is shown in panel (*a*). The velocity structure was calculated from Equation 1 shown in panel (*b*). The region where $C^{18}O$ arises is shown by hatching. Radial profiles of $\delta v_{\rm rot}$ from the midplane and the $C^{18}O$ emission region are shown in panel (*c*) by the gray and blue lines respectively.

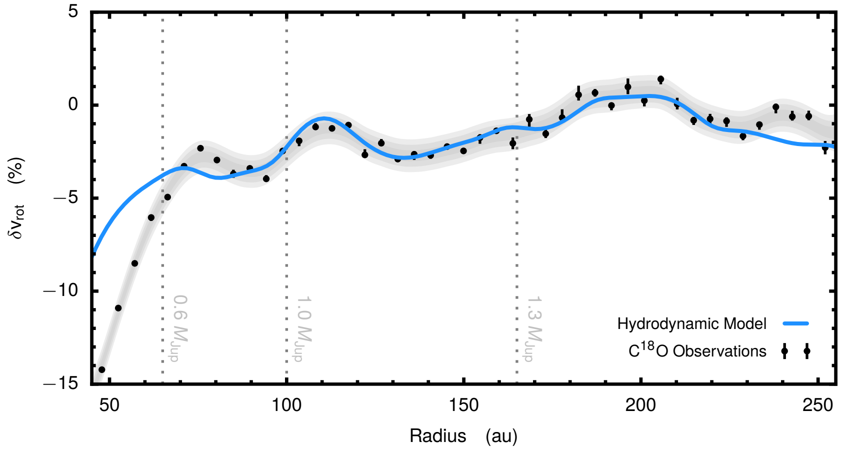

Figure 3: **Comparison of the best-fit model with observations.** Results from individual annuli are shown by black points with the Gaussian Process model with 3σ uncertainties shown by the gray band. The best fit model with 0.6, 1.0 and $1.3\ M_{\mathrm{Jup}}$ planets at 65, 100 and 165 au is shown by the blue line.

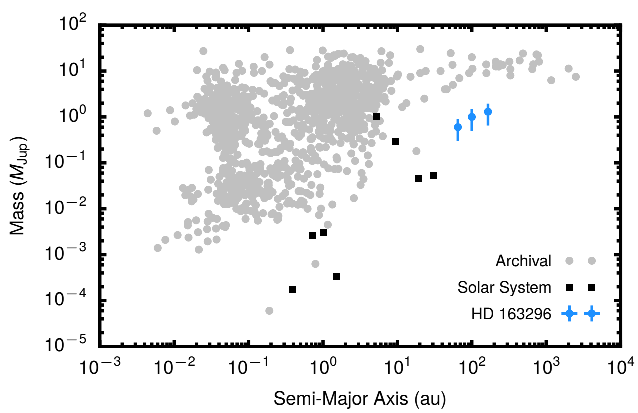

Figure 4: **Comparison with known planets.** Planets detected in HD 163296 shown in blue are probing a new regime in the planetary mass-orbit relation as shown by the confirmed planets in gray points taken from the NASA Exoplanet Archive[10]. Black squares mark the planets in the Solar System.

Methods

ALMA Observations This project used the archival data 2013.1.00601.S (PI: A. Isella[3]) which targeted ^{12}CO, ^{13}CO and C^{18}O emission at $\approx 0.25''$ spatial resolution and 15 kHz spectral resolution, equivalent to 20 $\mathrm{m\,s^{-1}}$. The data were calibrated using the scripts provided with the data and using the `CASA v4.0.0` pipeline. Using `CASA v5.1.1` and following the original work, the data were self-calibrated using the 232 GHz continuum window, before the continuum substraction using the `uvcontsub` task. Images were produced with a channel spacing of 50 $\mathrm{m\,s^{-1}}$ and a Briggs robust parameter of 0.5 resulting in beam sizes $\approx 0.28'' \times 0.23''$. The images were then rotated assuming a position angle of 132^o to align the major axes with the x-axis.

Emission Surfaces As molecular line emission arises from an elevated region above the midplane[31,32], the observed emission is asymmetric[21,33]. This asymmetry was used to derive the emission surface profiles which was used to properly deproject the data into azimuthal bins of constant radius.

We follow the method presented in Pinte et al.[22], producing multiple samples of the emission surface z as a function of r. Instead of binning the data, we model the emission surface as a Gaussian Process. This implicitly assumes that the underling function is smooth and takes into account both correlations in the data and in the noise. This model is implemented with `celerite` [34]. Figure 5 displays the derived surfaces for the three lines and the associated 3σ uncertainties of the GP model. We used both a simple harmonic oscillator kernel and a Matern 3/2 kernel, both times including a Jitter term to account for the scatter, and found comparable results.

The resulting emission surfaces agree qualitatively well with previous modelling predictions.

The ^{12}CO surface is comparable to the upper CO molecular layer in Rosenfeld et al.[21], while the $C^{18}O$ emission is comparable to that in the model of Flaherty et al.[29]. We note however that the observed ^{12}CO emission is somewhat higher than in the model which may suggest a limitation of the parametric structure used. $C^{18}O$ data clearly shows dips at the locations of the two outer continuum gaps at 100 au and 170 au, in addition to a third further out at 230 au, coincident with the outer gap in DCO^+ reported in Flaherty et al.[29]. The more optically thick lines of ^{12}CO and ^{13}CO show smoother, less perturbed surfaces.

For a vertical Gaussian profile for the density structure, a reasonable assumption for regions close to the midplane, the emission surface z_τ is given by,

$$z_\tau = \sqrt{2} H_{\rm gas} \cdot {\rm erfc}^{-1} \left(\frac{2 \left(x_{\rm mol} \cdot N_\tau + 1.3 \times 10^{21} \right)}{\Sigma_{\rm gas}} \right) \tag{2}$$

where N_τ is the observable column density of the emitting molecule required to reach an optical depth of τ, $x_{\rm mol}$ is the relative abundance of the emitting molecule with respect to H_2, $H_{\rm gas}$ is the pressure scale height of the gas and ${\rm erfc}^{-1}$ is the inverse complimentary error function. Assuming $x_{\rm mol} \cdot N_\tau$ remains constant across the gap locations, as suggested by the lack of features in Figure 1a, changes in the emission height must therefore require a drop in either, or a combination of, $H_{\rm gas}$, and thus the midplane temperature, or $\Sigma_{\rm gas}$.

As the disk is believed to have negligible non-thermal line broadening[28,29,35], the line width will directly trace the gas temperature. No deviations from a smooth profile are observed for $C^{18}O$ suggesting that the temperature traced across these gaps is relatively constant, as shown in Figure 7, thus a smooth profile for $H_{\rm gas}$ would be expect. Therefore pressure gradients changes would have to be predominantly driven by changes in $\Sigma_{\rm gas}$.

Rotation Profiles Calculation of $v_{\rm rot}$ takes advantage of the azimuthal symmetry of the disk. No significant azimuthal structure is observed for the HD 163296 disk in thermal continuum emisison, molecular line emission or scattered light emission[3,28,29,36,37]. For a given radius from the central star, the line profile will share the same properties; only the line centre should be Doppler shifted by the line-of-sight component of rotation. For an assumed $v_{\rm rot}$, each pixel can be shifted back to a common line centre and then the lines azimuthally stacked to improve the signal to noise[38–40].

Rather than assuming a rotation profile *a priori* to make this deprojection, one can be inferred. We assert that the correct rotation velocity is the one which results in the narrowest line profile for the stacked profile. Any error in the assumed rotation velocity will result in a slight offset in the line centres before stacking and thus lead to a broadening of the line. By deprojecting the lines to a common centre, we also effectively sample the true line profile at a much higher sampling rate than the correlator, allowing for a highly accurate calculation of the line width.

To derive $v_{\rm rot}$, each image cube was split into annuli with a width of 9 au (roughly two pixels), accounting for the derived emission surface. Although this is below the spatial resolution of the data, wider bins result in sampling a range of $v_{\rm Kep}$ values which can hide any signal from pressure gradients. As each annulus samples points from spatially uncorrelated pixels, the resulting correlation is less severe. Testing this procedure with a forward model with known rotation profiles demonstrated that no significant bias is introduced.

For each annulus, v_{rot} was calculated as the velocity profile which minimized the width of the line profile from the stacked, deprojected lines. This minimization used the `L-BFGS-B` method implemented in the `scipy.optimize` package. During this minimization, we also allowed the relative position angle to vary to account for possible uncertainties in the position angle. A similar approach has been used to model the Doppler shift due to binary stars.[41]. This approach was tested on mock data and was shown to robustly recover the rotation profile.

Figure 6 demonstrates the procedure with mock data. Here lines are assumed to have $\Delta V = 150~\mathrm{m\,s^{-1}}$ sampled at a $40~\mathrm{m\,s^{-1}}$ resolution, comparable to the observations. Each line is corrupted with white noise with a standard deviation of 10%, comparable to the data. An annulus of constant radius is shown in the left panel containing 40 lines, evenly spaced in azimuth. Shifting each spectrum by an amount $v_{\mathrm{rot}} \cdot \cos(\theta)$ results in a single line profile as shown in the centre panel resulting in sampling rate of roughly $2~\mathrm{m\,s^{-1}}$. A Gaussian profile is fit to the deprojected data, varying v_{rot} to minimize the line width. The line width as a function of v_{rot} is a convex function centred at the intrinsic line width, as shown in the right panel. The dashed lines show the recovered values for the mock data; both v_{rot} and ΔV were recovered to an accuracy of $2~\mathrm{m\,s^{-1}}$.

To calculate uncertainties for the derived v_{rot} profile, we used the deprojected spectra as the model, then used the Monte-Carlo Markov Chain (MCMC) sampler implemented in `emcee`[42] to sample the posterior distributions of v_{rot} and the position angle. The posterior distributions were uncorrelated and no significant deviation from zero for the position angle was found. 1σ uncertainties, calculated as the 16th to 84th percentiles of the posterior distribution, were found to agree with the simple minimization approach.

For the reference velocity profile we take a Keplerian profile assuming $i = 47.7^{\circ}$ around a $2.3\ M_{\rm sun}$ star. Residuals are calculated as $\delta v_{\rm rot} = 100 \times (v_{\rm rot} - v_{\rm Kep}) \,/\, v_{\rm Kep}$. Changes in the inclination or mass of the central star will result in a vertical offset for $\delta v_{\rm rot}$ so we are unable to determine if any gas rotation is truly super-Keplerian. Relative values, which trace local changes in the gas rotation, will remain unchanged.

The relative residual from $v_{\rm Kep}$ for the three lines is shown in Figure 8. The measurements are shown by the points while the solid line shows a Gaussian Process model. All uncertainties are 3σ. Each annulus is able to constrain $v_{\rm rot}$ to $\approx 2\ {\rm m\,s^{-1}}$, however the Gaussian Process model, which takes into account the entire radial profile and tries to find a smooth model to the observations, has uncertainties of $\approx 8\ {\rm m\,s^{-1}}$. All three lines show broadly comparable features, however $C^{18}O$ exhibits the most clear perturbations. Differences between lines suggest a change in the pressure profile as a function of height as well as radius.

The significant difference between the ^{12}CO and the more comparable ^{13}CO and $C^{18}O$ lines is likely due to the ^{12}CO emission tracing a much higher region in the disk as shown in Fig. 5. This demonstrates that we are able to trace perturbations in the disk physical structure in both radial and vertical directions. As full 3D models with fully-consistent temperature and density structures are beyond the scope of this paper, we limit ourselves to the comparison with the $C^{18}O$ emission which traces the region closest to the midplane and thus the region where simple parametric models are most applicable.

As deviations are observed in all three isotopologues, yet only significant changes in emission height observed in $C^{18}O$, we can rule out solely changes in the emission height as the cause for the osberved deviations. We therefore consider the scenario where the pressure gradient is significantly perturbed by the presence of a planet opened gap.

Hydrodynamic Models We carry out hydrodynamic simulations to estimate the masses and radial locations of planets responsible for the observed gas pressure gradient changes in the HD 163296 disk. We solve the hydrodynamic equations for mass and momentum conservation in the two-dimensional polar coordinates (r, θ) using FARGO 3D[43]. The orbital advection algorithm FARGO [44] is used in the calculations. We use 1024 logarithmic radial grid cells between 16 and 480 au, and 1920 uniform azimuthal grid cells covering full 2π radians.

The disk model is based on a parametric model[28,29] which has found a good fit to CO isotopologue emission. The initial density profile is described by,

$$\Sigma(r) = \Sigma_0 \left(\frac{r}{r_c}\right)^{-\gamma} \exp\left[-\left(\frac{r}{r_c}\right)^{2-\gamma}\right], \tag{3}$$

with $\gamma = 0.8$ and $r_c = 200$ au. The mass normalization constant is given by,

$$\Sigma_0 = (2-\gamma) \cdot \frac{M_{\rm gas}}{2\pi r_c^2} \cdot \exp\left[\left(\frac{r_{\rm in}}{r_c}\right)^{2-\gamma}\right]. \tag{4}$$

where $M_{\rm gas} = 0.09\ M_{\rm sun}$ and $r_{\rm in} = 20\ {\rm au}$. Since we use two-dimensional simulations to efficiently explore the parameter space, the temperature profile at the disk midplane is adopted, $T_{\rm mid}(r) = 21 \times (r/r_c)^{-0.3}$ K, along with an isothermal equation of state. We assume a uniform disk viscosity of $\alpha = 10^{-3}$, where α is a dimensionless parameter characterizing the efficiency of mass transport defined as in the canonical α prescription[45]. This choice is consistent with the constraints on the turbulence level in the HD 163296 disk[28,29].

An initial parameter study was performed using one planet at a time. We place a planet at either 105 or 160 au, which are the locations suggested by the continuum ring locations[3], and test four different planetary masses at each location: 0.1, 0.3, 1, and 3 $M_{\rm Jup}$. We insert planets at the beginning of simulations with their full masses. We have tests in which we begin simulations with 20 Earth-mass cores and grow them over time by accreting available disk material from their vicinity[46,47]. However, the final gap shapes are almost identical to the case we start with full planet masses. This is because the available masses around the planetary orbits in the HD 163296 disk are much larger than the planets' final masses, so that most of the disk material is pushed away by the planets and only small fraction is accreted.

We compare the difference between the minimum and maximum $\delta v_{\rm rot}$ values measured in numerical simulations with that obtained from the $C^{18}O$ observation. Using this approach, we find that both at 105 and 160 au a $1\ M_{\rm Jup}$ planet yields a reasonable match. Because of the lack of a $\delta v_{\rm rot}$ minimum at < 70 au in the $C^{18}O$ observation, we were not able to use the same approach for the innermost planet. We thus adopt $0.1\ M_{\rm Jup}$ as our initial attempt, as suggested by Isella et al.[3].

We then include all three planets and vary their masses by $0.1\ M_{\rm Jup}$ and their locations by 5 au to find our best-fit model: $0.6\ M_{\rm Jup}$ planet at 65 au, $1\ M_{\rm Jup}$ planet at 100 au, and $1.3\ M_{\rm Jup}$ planet at 165 au. The surface density and the gas rotation velocity are shown in Fig 9.

For this second part of the parameter study, we generate simulated $C^{18}O$ velocity profiles to compare these models with the observations. To do so, the surface densities obtained from hydrodynamic simulations were inflated to a full 3D structure using a commonly used parametric hydrostatic structure using the temperature structure from Flaherty et al.[29]. The $C^{18}O$ abundance was assumed to be 8.67×10^{-8} with a vertical distribution bounded by the freezeout temperature of 27 K to the bottom and a shielding column of 1.2×10^{21} H_2 cm^{-2} above[48]. The velocity structure was calculated using Eqn. 1. Radiative transfer was performed with the non-LTE code LIME[49] with image values matching the observation. As we do not expect significant spatial filtering from the data[3], the images were convolved with a 2D Gaussian beam consistent with the $C^{18}O$ observations to provide a fair comparison. We limit ourselves to comparison with only $C^{18}O$ because in the upper layers, where ^{12}CO is observed to arise, the assumed parametric structure deviates significantly from self-consistently calculated physical structures[50].

Using this iterative process between hydrodynamic simulations and radiative transfer calculations, we were able to constrain the planetary masses and the radial locations within ± 50 % and ± 10 %, respectively. Figure 10 demonstrates how the δv_{rot} profile changes with these uncertainties. We note that these masses are considerably larger than those estimated from the continuum gaps[3] as the method presented here does not require poorly known relative abundances and is directly tracing the gas pressure.

The value of δv_{rot} at the planet locations is not zero due to the global pressure gradient from the radially decreasing temperature and density, and the non-negligible height of the $C^{18}O$ emission. This can be clearly seen in panel (*c*) of Figure 2 where $\delta v_{\mathrm{rot}} \approx -2\%$ at the planet locations, consistent with the observations.

As when fitting the continuum gaps[3], no perfect fit with a planet could be found for the perturbation at < 80 au. Using a $0.6\ M_{\rm Jup}$ planet at 65 au provided a reasonable fit but was unable to fully account for the sharp deviation in $\delta v_{\rm rot}$. It appears from Figure 10 that pushing the innermost planet outward could produce a $\delta v_{\rm rot}$ peak at 75 au; however, locating a planet at ≥ 70 au resulted in the formation of a single, wide gap together with the planet at 100 au, rather than the formation of two separate gaps. Even with α ranging between 0 and 10^{-3}, no reasonable fit was found.

We have also examined a possibility that the secondary spiral arm excited by the planet at 100 au opens a secondary gap at ~ 70 au. The location of secondary gap is determined mainly by the disk temperature and the planetary mass[9], and for the disk temperature assumed in the present work we found that a secondary gap forms with $\alpha \lesssim 10^{-4}$, but at $< \ 65$ au regardless of the planetary mass.

The rapid drop in $\delta v_{\rm rot}$ at < 75 au might indicate a rapid increase in gas density there, which could potentially be associated with radially varying accretion efficiency in the disk. Recent radiative transfer modelling of scattered light images of the HD 163296 disk indeed supports this idea of rapid gas density increase inside of the innermost gap[37]. Future higher resolution observations will help better understand the origin of the innermost gap.

1. ALMA Partnership *et al.* The 2014 ALMA Long Baseline Campaign: First Results from High Angular Resolution Observations toward the HL Tau Region. *ApJL* **808**, L3 (2015). `1503.02649`.

2. Andrews, S. M. *et al.* Ringed Substructure and a Gap at 1 au in the Nearest Protoplanetary Disk. *ApJL* **820**, L40 (2016). `1603.09352`.

3. Isella, A. *et al.* Ringed Structures of the HD 163296 Protoplanetary Disk Revealed by ALMA. *Physical Review Letters* **117**, 251101 (2016).

4. Fedele, D. *et al.* ALMA unveils rings and gaps in the protoplanetary system HD 169142: signatures of two giant protoplanets. *A&A* **600**, A72 (2017). `1702.02844`.

5. Zhang, K., Blake, G. A. & Bergin, E. A. Evidence of Fast Pebble Growth Near Condensation Fronts in the HL Tau Protoplanetary Disk. *ApJL* **806**, L7 (2015). `1505.00882`.

6. Flock, M. *et al.* Gaps, rings, and non-axisymmetric structures in protoplanetary disks. From simulations to ALMA observations. *A&A* **574**, A68 (2015). `1411.2736`.

7. Birnstiel, T., Andrews, S. M., Pinilla, P. & Kama, M. Dust Evolution Can Produce Scattered Light Gaps in Protoplanetary Disks. *ApJL* **813**, L14 (2015). `1510.05660`.

8. Okuzumi, S., Momose, M., Sirono, S.-i., Kobayashi, H. & Tanaka, H. Sintering-induced Dust Ring Formation in Protoplanetary Disks: Application to the HL Tau Disk. *ApJ* **821**, 82 (2016). `1510.03556`.

9. Bae, J., Zhu, Z. & Hartmann, L. On the Formation of Multiple Concentric Rings and Gaps in Protoplanetary Disks. *ApJ* **850**, 201 (2017). `1706.03066`.

10. Akeson, R. L. *et al.* The NASA Exoplanet Archive: Data and Tools for Exoplanet Research. *PASP* **125**, 989 (2013). `1307.2944`.

11. Kraus, A. L. & Ireland, M. J. LkCa 15: A Young Exoplanet Caught at Formation? *ApJ* **745**, 5 (2012). `1110.3808`.

12. Quanz, S. P. *et al.* A Young Protoplanet Candidate Embedded in the Circumstellar Disk of HD 100546. *ApJL* **766**, L1 (2013). `1302.7122`.

13. Sallum, S. *et al.* Accreting protoplanets in the LkCa 15 transition disk. *Nature* **527**, 342–344 (2015). `1511.07456`.

14. Currie, T. *et al.* Resolving the HD 100546 Protoplanetary System with the Gemini Planet Imager: Evidence for Multiple Forming, Accreting Planets. *ApJL* **814**, L27 (2015). `1511.02526`.

15. van der Marel, N. *et al.* A Major Asymmetric Dust Trap in a Transition Disk. *Science* **340**, 1199–1202 (2013). `1306.1768`.

16. Bergin, E. A. *et al.* An old disk still capable of forming a planetary system. *Nature* **493**, 644–646 (2013). `1303.1107`.

17. Bryden, G., Chen, X., Lin, D. N. C., Nelson, R. P. & Papaloizou, J. C. B. Tidally Induced Gap Formation in Protostellar Disks: Gap Clearing and Suppression of Protoplanetary Growth. *ApJ* **514**, 344–367 (1999).

18. Rosotti, G. P., Juhasz, A., Booth, R. A. & Clarke, C. J. The minimum mass of detectable planets in protoplanetary discs and the derivation of planetary masses from high-resolution observations. *MNRAS* **459**, 2790–2805 (2016). `1603.02141`.

19. Kanagawa, K. D. *et al.* Mass constraint for a planet in a protoplanetary disk from the gap width. *PASJ* **68**, 43 (2016). `1603.03853`.

20. Kanagawa, K. D. *et al.* Mass Estimates of a Giant Planet in a Protoplanetary Disk from the Gap Structures. *ApJL* **806**, L15 (2015). `1505.04482`.

21. Rosenfeld, K. A., Andrews, S. M., Hughes, A. M., Wilner, D. J. & Qi, C. A Spatially Resolved Vertical Temperature Gradient in the HD 163296 Disk. *ApJ* **774**, 16 (2013). `1306.6475`.

22. Pinte, C. *et al.* Direct mapping of the temperature and velocity gradients in discs. Imaging the vertical CO snow line around IM Lupi. *A&A* **609**, A47 (2018). `1710.06450`.

23. Pinilla, P., Flock, M., Ovelar, M. d. J. & Birnstiel, T. Can dead zones create structures like a transition disk? *A&A* **596**, A81 (2016). `1610.02044`.

24. Johansen, A., Youdin, A. & Klahr, H. Zonal Flows and Long-lived Axisymmetric Pressure Bumps in Magnetorotational Turbulence. *ApJ* **697**, 1269–1289 (2009). `0811.3937`.

25. Dittrich, K., Klahr, H. & Johansen, A. Gravoturbulent Planetesimal Formation: The Positive Effect of Long-lived Zonal Flows. *ApJ* **763**, 117 (2013). 1211.2095.

26. Bai, X.-N. & Stone, J. M. Magnetic Flux Concentration and Zonal Flows in Magnetorotational Instability Turbulence. *ApJ* **796**, 31 (2014). 1409.2512.

27. Flock, M. *et al.* Radiation Hydrodynamical Turbulence in Protoplanetary Disks: Numerical Models and Observational Constraints. *ApJ* **850**, 131 (2017). 1710.06007.

28. Flaherty, K. M. *et al.* Weak Turbulence in the HD 163296 Protoplanetary Disk Revealed by ALMA CO Observations. *ApJ* **813**, 99 (2015). 1510.01375.

29. Flaherty, K. M. *et al.* A Three-dimensional View of Turbulence: Constraints on Turbulent Motions in the HD 163296 Protoplanetary Disk Using DCO^+. *ApJ* **843**, 150 (2017). 1706.04504.

30. Tilling, I. *et al.* Gas modelling in the disc of HD 163296. *A&A* **538**, A20 (2012). 1111.2549.

31. Pavlyuchenkov, Y. *et al.* Molecular Line Radiative Transfer in Protoplanetary Disks: Monte Carlo Simulations versus Approximate Methods. *ApJ* **669**, 1262–1278 (2007). 0707.2905.

32. Semenov, D., Pavlyuchenkov, Y., Henning, T., Wolf, S. & Launhardt, R. Chemical and Thermal Structure of Protoplanetary Disks as Observed with ALMA. *ApJL* **673**, L195 (2008). 0801.1463.

33. de Gregorio-Monsalvo, I. *et al.* Unveiling the gas-and-dust disk structure in HD 163296 using ALMA observations. *A&A* **557**, A133 (2013). 1307.1357.

34. Foreman-Mackey, D., Agol, E., Angus, R. & Ambikasaran, S. Fast and scalable gaussian process modeling with applications to astronomical time series. *AJ* **154**, 220 (2017). URL https://arxiv.org/abs/1703.09710.

35. Hughes, A. M., Wilner, D. J., Andrews, S. M., Qi, C. & Hogerheijde, M. R. Empirical Constraints on Turbulence in Protoplanetary Accretion Disks. *ApJ* **727**, 85 (2011). 1011.3826.

36. Monnier, J. D. *et al.* Polarized Disk Emission from Herbig Ae/Be Stars Observed Using Gemini Planet Imager: HD 144432, HD 150193, HD 163296, and HD 169142. *ApJ* **838**, 20 (2017). 1702.04780.

37. Muro-Arena, G. A. *et al.* Dust modeling of the combined ALMA and SPHERE datasets of HD163296. Is HD163296 really a Meeus group II disk? *ArXiv e-prints* (2018). 1802.03328.

38. Teague, R. *et al.* Measuring turbulence in TW Hydrae with ALMA: methods and limitations. *A&A* **592**, A49 (2016). 1606.00005.

39. Yen, H.-W. *et al.* Stacking Spectra in Protoplanetary Disks: Detecting Intensity Profiles from Hidden Molecular Lines in HD 163296. *ApJ* **832**, 204 (2016). 1610.01780.

40. Matrà, L. *et al.* Detection of Exocometary CO within the 440 Myr Old Fomalhaut Belt: A Similar $CO+CO_2$ Ice Abundance in Exocomets and Solar System Comets. *ApJ* **842**, 9 (2017). 1705.05868.

41. Czekala, I. *et al.* Disentangling Time-series Spectra with Gaussian Processes: Applications to Radial Velocity Analysis. *ApJ* **840**, 49 (2017). 1702.05652.

42. Foreman-Mackey, D., Hogg, D. W., Lang, D. & Goodman, J. emcee: The mcmc hammer. *PASP* **125**, 306–312 (2013). 1202.3665.

43. Benítez-Llambay, P. & Masset, F. S. FARGO3D: A New GPU-oriented MHD Code. *ApJS* **223**, 11 (2016). 1602.02359.

44. Masset, F. FARGO: A fast eulerian transport algorithm for differentially rotating disks. *A&AS* **141**, 165–173 (2000). astro-ph/9910390.

45. Shakura, N. I. & Sunyaev, R. A. Black holes in binary systems. Observational appearance. *A&A* **24**, 337–355 (1973).

46. Kley, W. Mass flow and accretion through gaps in accretion discs. *MNRAS* **303**, 696–710 (1999). astro-ph/9809253.

47. Dürmann, C. & Kley, W. The accretion of migrating giant planets. *A&A* **598**, A80 (2017). 1611.01070.

48. Visser, R., van Dishoeck, E. F. & Black, J. H. The photodissociation and chemistry of CO isotopologues: applications to interstellar clouds and circumstellar disks. *A&A* **503**, 323–343 (2009). 0906.3699.

49. Brinch, C. & Hogerheijde, M. R. LIME - a flexible, non-LTE line excitation and radiation transfer method for millimeter and far-infrared wavelengths. *A&A* **523**, A25 (2010). 1008.1492.

50. Teague, R. *et al.* A Surface Density Perturbation in the TW Hydrae Disk at 95 au Traced by Molecular Emission. *ApJ* **835**, 228 (2017). 1702.02147.

Data availability This paper makes use of the following ALMA data: JAO.ALMA#2013.1.00601.S, available http://almascience.org/aq?project_code=2013.1.00601.S and from the corresponding author on reasonable request.

Acknowledgements ALMA is a partnership of European Southern Observatory (ESO) (representing its member states), National Science Foundation (USA), and National Institutes of Natural Sciences (Japan), together with National Research Council (Canada), National Science Council and Academia Sinica Institute of Astronomy and Astrophysics (Taiwan), and Korea Astronomy and Space Science Institute (Korea), in cooperation with Chile. The Joint ALMA Observatory is operated by ESO, Associated Universities, Inc/National Radio Astronomy Observatory (NRAO), and National Astronomical Observatory of Japan. The National Radio Astronomy Observatory is a facility of the National Science Foundation operated under cooperative agreement by Associated Universities, Inc. T.B. acknowledges funding from the European Research Council (ERC) under the European Unions Horizon 2020 research and innovation programme under grant agreement No 714769. J.B. acknowledges support from NASA grant NNX17AE31G and computing resources provided by the NASA High-End Computing (HEC) Program through the NASA Advanced Supercomputing (NAS) Division at Ames Research Center.

Author Contributions R.D.T. reduced the ALMA data and J.B. ran the hydrodynamic simulations. R.D.T. wrote the manuscript with revisions from E.A.B. All authors were participants in the discussion of results, determination of the conclusions and revision of the manuscript.

Author Informations Reprints and permissions information is available on request. The authors declare no competing financial interests. Readers are welcome to comment on the online version of the paper. Correspondence and requests for materials should be addressed to R.D.T. (email: rteague@umich.edu).

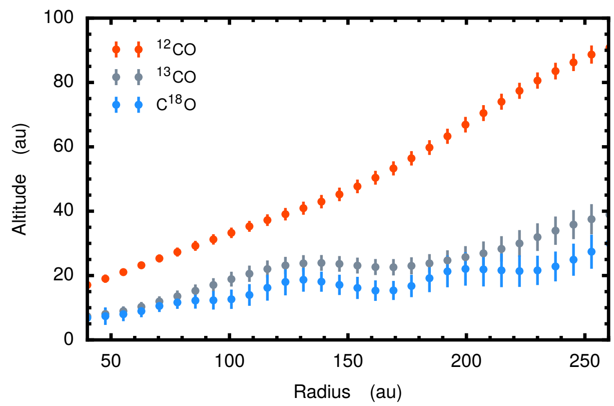

Figure 5: **Emission surfaces for the three CO isotopologues**. Derived following the method presented in [22]. Error bars show the 3σ uncertainties.

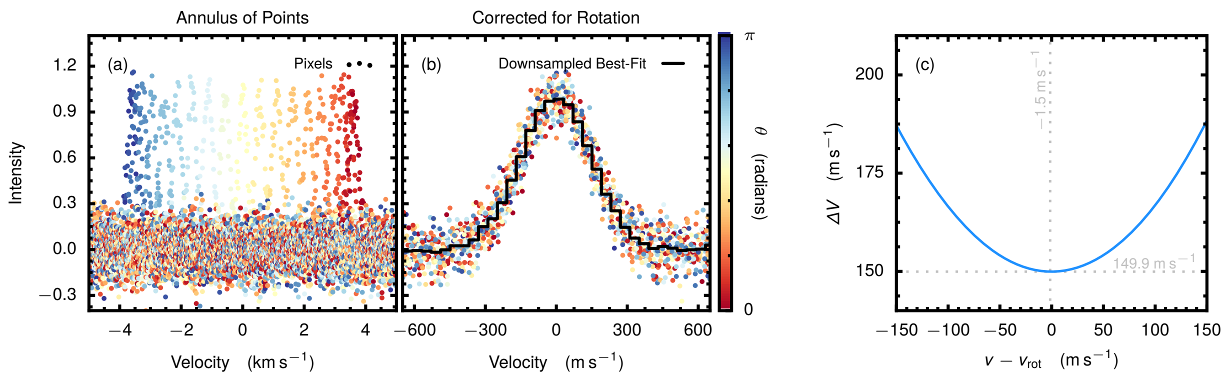

Figure 6: **Demonstration of the method used to calculate $v_{\rm rot}$.** Panel (a) shows the pixel values taken from an annulus of constant radius. Intrinsic line widths are $150\ {\rm m\,s^{-1}}$ sampled at $40\ {\rm m\,s^{-1}}$. Correcting for the rotation, the points align to a single Gaussian as shown in panel (b), sampling the profile at a rate of $\approx 2\ {\rm m\,s^{-1}}$. Colours of the points show their relative position angle in the disk. The black line shows the best-fit Gaussian profile, binned back down to the native velocity resolution. The line width is a convex function of rotation velocity as shown in panel (c). The dotted lines show the values where line width is minimized demonstrating that both $v_{\rm rot}$ and line width are recovered to $< 2\ {\rm m\,s^{-1}}$.

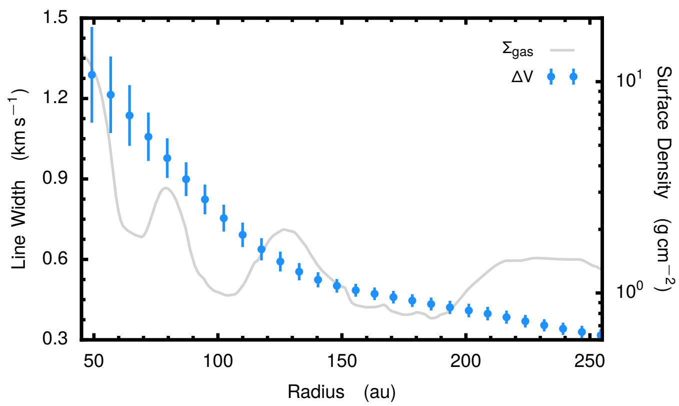

Figure 7: **Line width of the $C^{18}O$ emission.** No significant deviations from the rotational profile of the line width (shown by blue points with 3σ uncertainties) are observed across the surface density perturbations, shown by the gray solid line, suggesting a smooth temperature profile across the gaps.

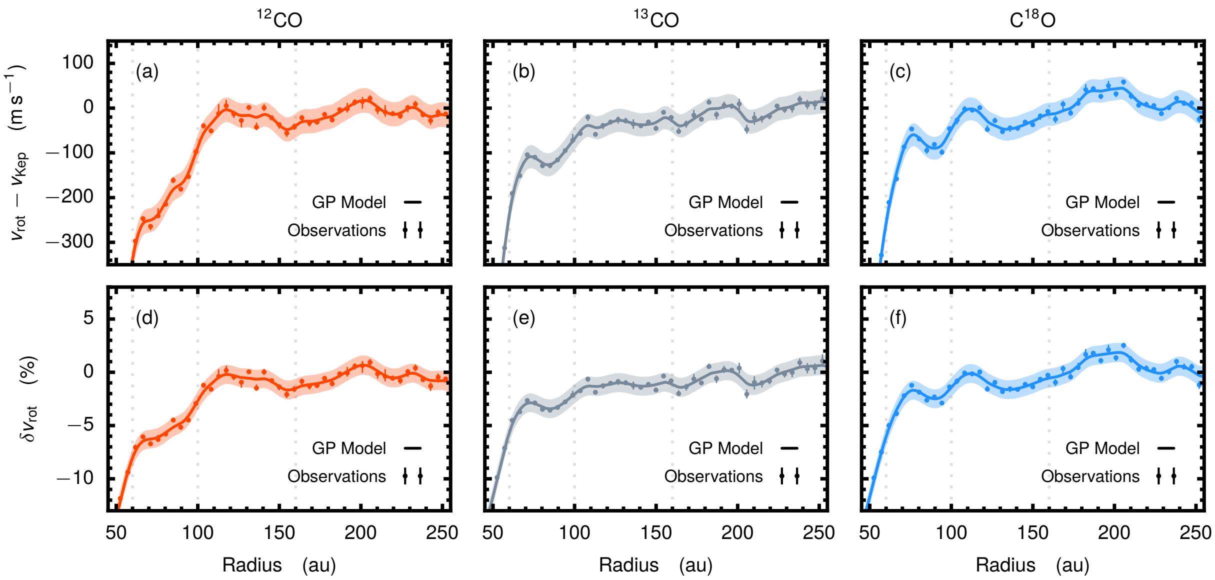

Figure 8: **Rotation velocities for the three CO isotopologues.** ^{12}CO, left; ^{13}CO, middle and $C^{18}O$, right. The top row shows the difference from $v_{\rm Kep}$ and the bottom row shows the relative difference. Observations are shown by the points with 3σ uncertainties. The solid line and shaded region are the Gaussian Process model and associated 3σ uncertainty. The dark rings in continuum emission are shown by the dashed lines.

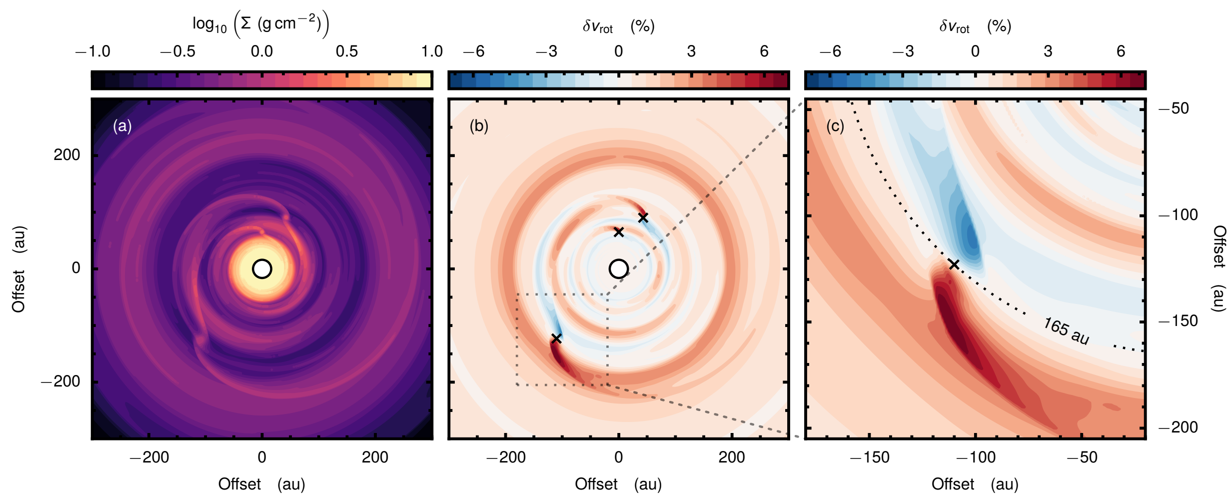

Figure 9: **Surface density and velocity structure of the hydrodynamical model.** The surface density is shown in the left panel while the centre shows $\delta v_{\rm rot}$ at the midplane. Planet locations are shown with a cross. The right panel shows a zoom in of the outer planet, showing the details of the sub- and super-Keplerian rotation inwards and outwards of the gap.

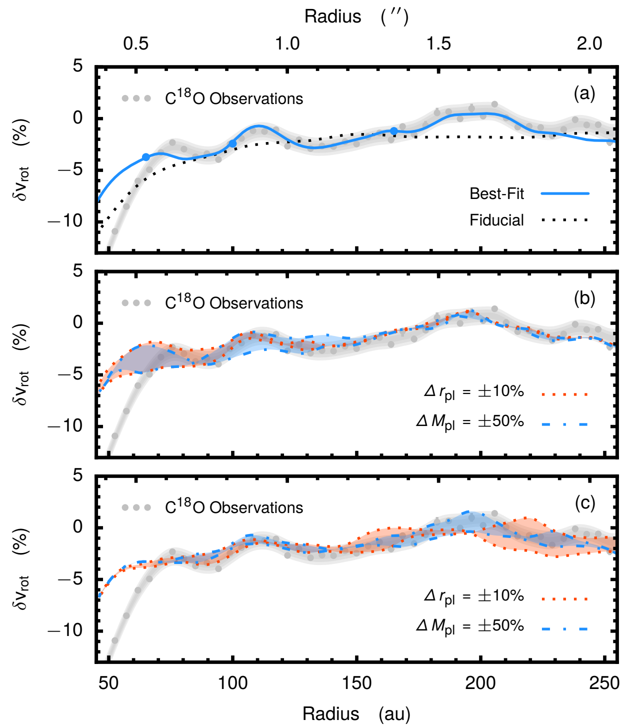

Figure 10: **Sensitivity of $\delta v_{\rm rot}$ to planetary parameters.** The best-fit hydrodynamical model is shown with the blue line overlaid to the observations in panel (a). The gray region shows the 3σ range of the Gaussian Processes model of the observations. The black dotted lines shows $v_{\rm rot}$ for the fiducial model, showing the fall off at small radii is due to the imaging. Panels (b) and (c) demonstrate the sensitivity of $\delta v_{\rm rot}$ to changes in planet mass and position for the planet at 100 au and 160 au, respectively. The red shaded region shows the changes in $\delta v_{\rm rot}$ with a 10% change in the radial location of the planet while the blue shaded regions show the change from a 50% change in planet mass. For panels (b) and (c), only one planet is moved at a time.